International Journal of Solids and Structures 49 (2012) 3291–3300

Contents lists available at SciVerse ScienceDirect

International Journal of Solids and Structures

journal homepage: www.elsevier.com/locate/ijsolstr

High strain-rate modeling of the interfacial effects of dispersed particles in high strength aluminum alloys

W.M. Lee, M.A. Zikry *

Department of Mechanical and Aerospace Engineering, North Carolina State University, Raleigh, NC 27695-7910, USA

ARTICLE INFO

Article history:
Received 3 September 2011
Received in revised form 21 June 2012
Available online 20 July 2012

Keywords:
Dispersoid
Aluminum alloy
High strain-rate
Orowan looping
Finite element method

ABSTRACT

The interfacial effects of dispersed particles on the dynamic deformation of high strength aluminum alloys have been investigated using an eigenstrain-based formulation coupled with dislocation-density based crystalline plasticity and a microstructurally based finite element framework. This accounts for the unrelaxed plastic strains associated with the interfacial behavior of dispersed particles, such as Orowan looping. Particle spacing had a significant effect on the distribution of plastic shear slip, with localization occurring between the particles for smaller particle spacing. The eigenstress field associated with larger particles led to longer-range interaction of pressure fields, which can promote void coalescence for nucleated voids at the particle-matrix interface. Grain orientation also had a significant effect on the behavior associated with the particles, with plastic shear slip localizing at the particle-matrix interfaces for low angle grain-boundary (GB) misorientations, and at GBs and GB junctions for high angle GB misorientations.

1. Introduction

In alloys subjected to high strain rates of strain, the distribution and morphology of precipitates, dispersed particles, and matrix grains, and the interaction of propagating waves with these microstructure features at the different length scales, are critical in the optimization of strength, toughness, and ductility. The addition of Mn to quaternary Al–Cu–Mg–Ag alloys leads to improvements in toughness and ductility due to the formation of orthorhombic, rod-like $Al_{20}Cu_2Mn_3$ dispersed particles (Cho and Bes, 2006), generally larger than 100 nm along the long axis (Lee and Zikry, 2011a). The increase in toughness has been attributed to reduced planar slip (Cho and Bes, 2006), and the increase in ductility has been attributed to particle-controlled slip, which can promote transgrannular failure (Starke and Sanders, 1980).

The interaction of dislocations with these dispersed particles clearly affects the behavior of high strength aluminum alloys when subjected to extreme loading conditions, as these particles have been observed on fracture surfaces of Al 2139 plates subjected to ballistic loading (Lee and Zikry, 2011a) and Al 2139 samples deformed by split Hopkinson pressure bar impact experiments. However, the evolution of the dislocation interactions with dispersed particles, such as Orowan loop formation, is difficult, if not impossible, to capture experimentally, especially under dynamic deformation, due to the time scales associated with Orowan looping under dynamic deformation and the ability of the loops to anneal out of TEM samples (Humphreys and Stewart, 1972; Salem et al., 2012).

Accurate modeling techniques that can predict the effects of the dislocation interactions with these particles on the behavior of the alloys are therefore essential in understanding the effects of dispersed particles on the evolution of the deformation when the material is subjected to high strain rate loading. However, atomistic simulation (Bacon and Osetsky, 2005, 2007; Shim et al., 2008; Kohler et al., 2005; Hatano, 2008) and dislocation dynamics (Takahashi, 2008; Queyreau and Devincre, 2009) approaches are generally severely restricted by length and temporal scale limitations. Dislocation density based crystalline plasticity can overcome these length and temporal scale limitations (Bate, 1999; Elkhodary et al., 2011). However, the interactions of dislocations and dispersed particles must be accounted for, since the deformation is restricted in matrix elements adjacent to particle elements if the interface intersects the slip plane.

Therefore, we have used an eigenstrain representation of Orowan looping coupled with dislocation density based crystalline plasticity and a specialized finite element framework to model the unrelaxed plastic strain and interfacial behavior associated with dispersed particles in high strength aluminum alloys. These eigenstrains, as noted by Mura (1987), are inelastic strains, and the incompatibilities of these eigenstrains can lead to eigenstress fields. Relaxation of these eigenstrains is accounted for by the incompatibilities of the lattice rotations of the particle and matrix that occur due to dislocation generation in the matrix that relaxes the Orowan loops (Humphreys, 1979).

* Corresponding author. Tel.: +1 919 515 5237; fax: +1 919 515 7968.
E-mail addresses: zikry@ncsu.edu, zikry@eos.ncsu.edu (M.A. Zikry).

0020-7683/$ - see front matter © 2012 Elsevier Ltd. All rights reserved.
http://dx.doi.org/10.1016/j.ijsolstr.2012.07.003

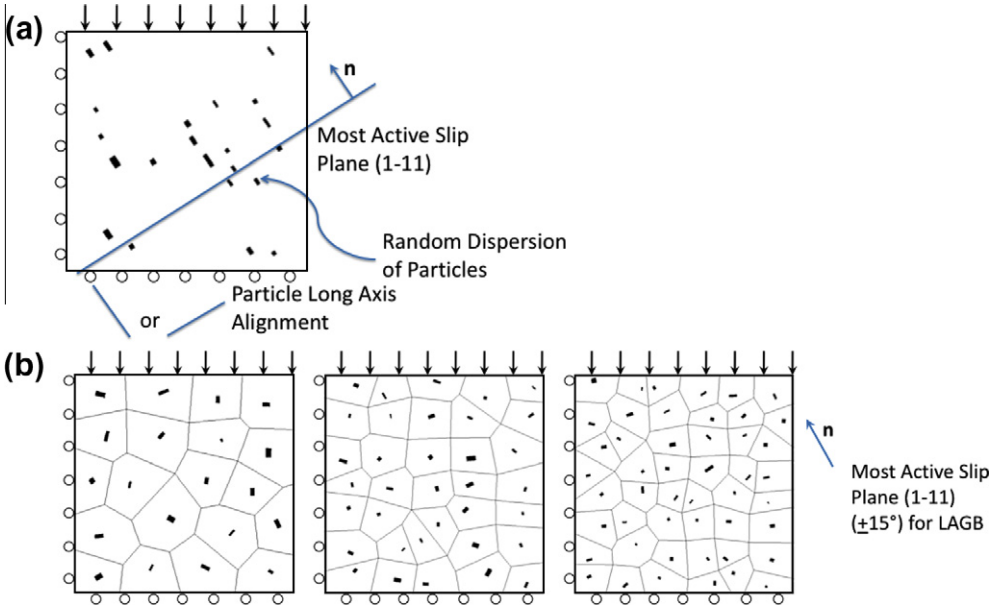

Fig. 1. Summary of the investigated models: (a) 20 μm by 20 μm single grain with random dispersions of particles and (b) 20 μm by 20 μm polycrystalline aggregate with 20, 35, and 48 grains and with one dispersed particle per grain.

Table 1
Grain misorientation averages for polycrystalline aggregates (degrees).

	Low angle GB misorientations	High angle GB misorientations
20-Grain	12.9399	38.6500
35-Grain	13.0177	38.9619
48-Grain	12.8471	37.8406

Table 2
Material properties of aluminum matrix and manganese-bearing dispersed particles.

Property	Matrix value	Particle value
Elastic modulus, E	70 GPa	110 GPa
Poisson's ratio, v	0.33	0.33
Static yield strength, τ^{α}	200 MPa	∞
Rate sensitivity, m	0.01	N/A
Reference strain rate, $\dot{\gamma}_{ref}$	0.001 s^{-1}	N/A
Burgers vector, $\vec{b}_v$	0.289 × {111}<110> nm	N/A
Initial ρ_m	10^{11} m^{-2}	N/A
Initial ρ_{im}	10^{13} m^{-2}	N/A
Saturation ρ_{im}	10^{14} m^{-2}	N/A

The major objective of this investigation is to use this formulation investigate the effects of particle dispersion, orientation, and sizing, along with matrix grain orientation, on the performance of a high strength aluminum alloy subjected to high strain rate compressive loading conditions, with an emphasis on delineating the effects of these particles on possible failure modes, such as shear strain localization and particle/matrix interfacial stress accumulations, which can lead to void nucleation and debonding at particle-matrix interfaces.

2. Approach

2.1. Dislocation density based crystalline plasticity

The constitutive formulation for rate-dependent multiple-slip crystal plasticity, coupled to evolutionary equations for the dislocation densities, will be outlined below. For a detailed presentation, see Zikry and Kao (1996) and Ashmawi and Zikry (2000).

It is assumed that the velocity gradient can be additively decomposed into elastic and plastic parts, L^e_{ij} and L^p_{ij}. These will be further decomposed into the symmetric deformation rate tensors, D^e_{ij} and D^p_{ij}, and antisymmetric spin tensors, W^e_{ij} and W^p_{ij}. The plastic parts are related to the crystallographic slip rates as

$$D^p_{ij} = P^{(\alpha)}_{ij}\dot{\gamma}^{(\alpha)}, \quad W^p_{ij} = \omega^{(\alpha)}_{ij}\dot{\gamma}^{(\alpha)}, \tag{1}$$

where α is summed over all slip-systems, and $P^{(\alpha)}_{ij}$ and $\omega^{(\alpha)}_{ij}$ are the symmetric and antisymmetric parts of the Schmid tensor, defined in terms of the slip planes and directions. As a measure of strain, the effective plastic shear slip is calculated from the plastic deformation rate tensor as

$$\gamma_{eff} = \frac{2}{3}\int \sqrt{D^p_{ij}D^p_{ij}}dt. \tag{2}$$

Power law hardening is assumed, relating the slip rates on the various slip systems to the resolved shear stress as

$$\dot{\gamma}^{(\alpha)} = \dot{\gamma}^{(\alpha)}_{ref}\left[\frac{\tau^{(\alpha)}}{\tau^{\alpha}_{ref}}\right]\left[\frac{|\tau^{(\alpha)}|}{\tau^{\alpha}_{ref}}\right]^{(1/m)-1} \quad \text{no sum on } \alpha, \tag{3}$$

where $\dot{\gamma}^{(\alpha)}_{ref}$ is the reference shear strain rate which corresponds to a reference shear stress, τ^{α}_{ref}, and m is the strain-rate sensitivity parameter. The reference shear stress is given by the following, accounting for thermal softening and forest hardening associated with the immobile dislocation density,

$$\tau^{\alpha}_{ref} = \left(\tau^{\alpha}_{s} + \mu b\sum_{j=1,nss}\sqrt{a_{\alpha j}\rho^{j}_{im}}\right)\left(\frac{T}{T_r}\right)^{\zeta} \tag{4}$$

where T_r is the reference temperature, 293 K, τ^{α}_{s} is the static yield stress of the matrix slip planes, which can be influenced by the presence of smaller nanoscale precipitates in high strength aluminum alloys, ζ is the thermal softening exponent, taken as −0.3, and $a_{\alpha j}$ accounts for the interaction between slip systems.

For high strain-rate investigations under the assumption of adiabatic heating, the temperature is updated using

$$\dot{T} = \frac{\chi}{\rho c_p}\sigma'_{ij}D^p_{ij}, \tag{3.11}$$

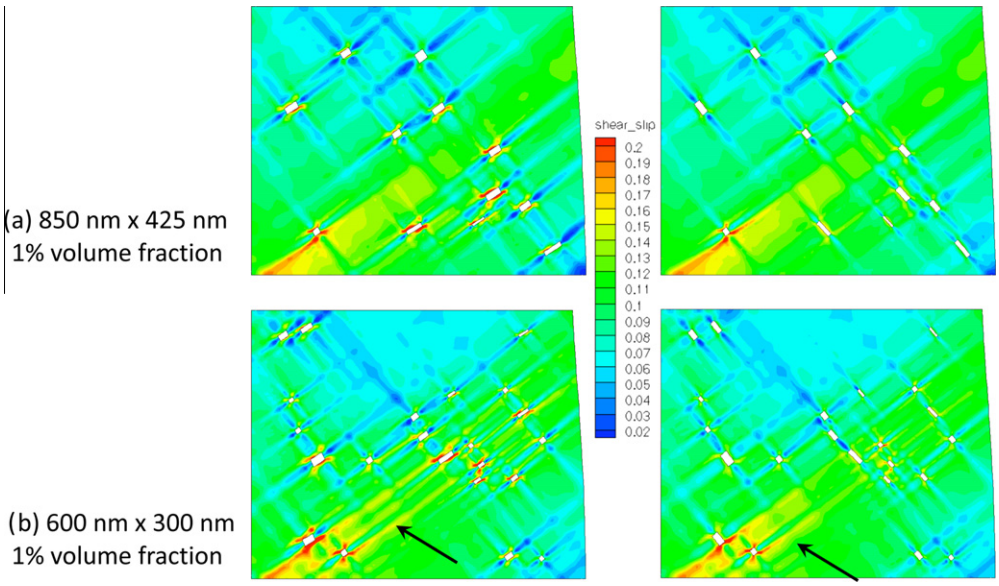

Fig. 2. Effective plastic slip contours in the matrix at 10% nominal compressive strain for 1.0% volume fraction of particles in a single crystal at a strain rate of $50 \times 10^{-3}\ s^{-1}$: (a) 800 nm by 425 nm average dispersed particle size and (b) 600 nm by 300 average dispersed particle size. Arrows indicate banded slip.

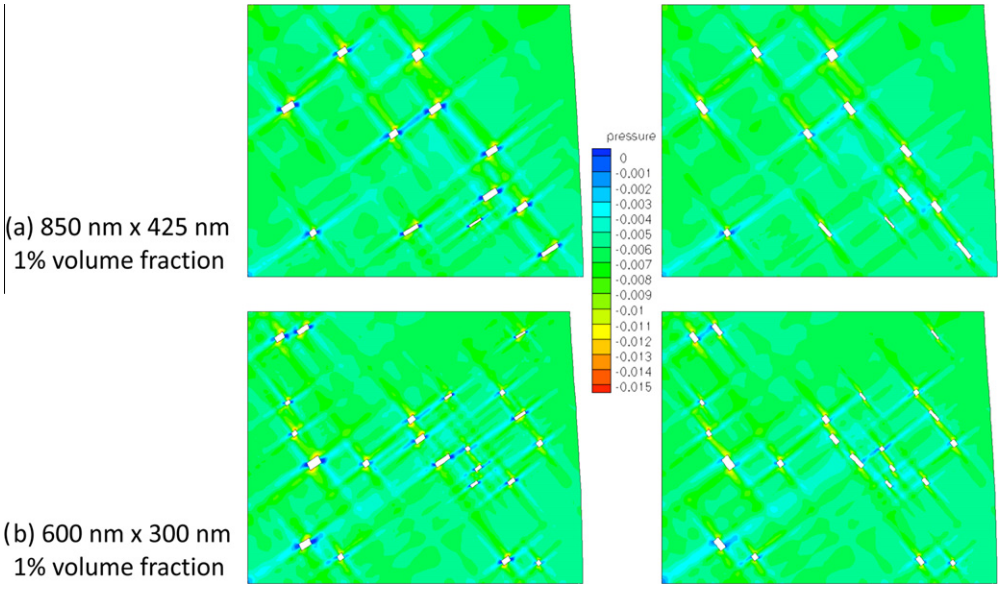

Fig. 3. Pressure contours in the matrix (normalized by the matrix Young's modulus) at 10% nominal compressive strain for 1.0% volume fraction of particles in a single crystal: (a) 800 nm by 425 nm average dispersed particle size and (b) 600 nm by 300 average dispersed particle size. Contour levels set to emphasize decrease in compressive pressures and transition to tensile pressures at the particle-matrix interface.

where χ is the fraction of plastic work converted to heat, which is approximately 0.9, ρ is the mass density, c_p is the specific heat of the material, and σ'_{ij} is the deviatoric stress.

It will be assumed that the total dislocation density can be decomposed additively into mobile and immobile parts. The evolutionary equations (Kameda and Zikry, 1998) associated with these components are given as

$$\frac{d\rho^{\alpha}_{m}}{dt} = |\dot{\gamma}^{\alpha}|\left(\frac{g^{\alpha}_{sour}}{b^2}\left(\frac{\rho^{\alpha}_{im}}{\rho^{\alpha}_{m}}\right) - g^{\alpha}_{mnter-}\rho^{\alpha}_{m} - \frac{g^{\alpha}_{immob-}}{b}\sqrt{\rho^{\alpha}_{im}}\right), \tag{5a}$$

$$\frac{d\rho^{\alpha}_{im}}{dt} = |\dot{\gamma}^{\alpha}|\left(g^{\alpha}_{mnter+}\rho^{\alpha}_{m} + \frac{g^{\alpha}_{immob+}}{b}\sqrt{\rho^{\alpha}_{im}} - g^{\alpha}_{recov}\rho^{\alpha}_{im}\right). \tag{5b}$$

The coefficients are not known a priori, but evolve with plastic deformation of the material. These are based off of energetically favorable interactions that occur in metals, such as those associated with Frank-Read sources, dislocation trapping, immobilization, and annihilation. For a detailed derivation, see Shanthraj and Zikry (2011).

$$g^{\alpha}_{sour} = b^{\alpha} f \varphi \sum_{\beta} \sqrt{\rho^{\beta}_{im}}, \tag{6a}$$

$$g^{\alpha}_{mnter-} = l_c f_0 \sum_{\beta}\left[\frac{\rho^{\beta}_{m}}{\rho^{\alpha}_{m} b^{\alpha}} + \frac{\dot{\gamma}^{\beta}}{\dot{\gamma}^{\alpha} b^{\beta}}\right], \tag{6b}$$

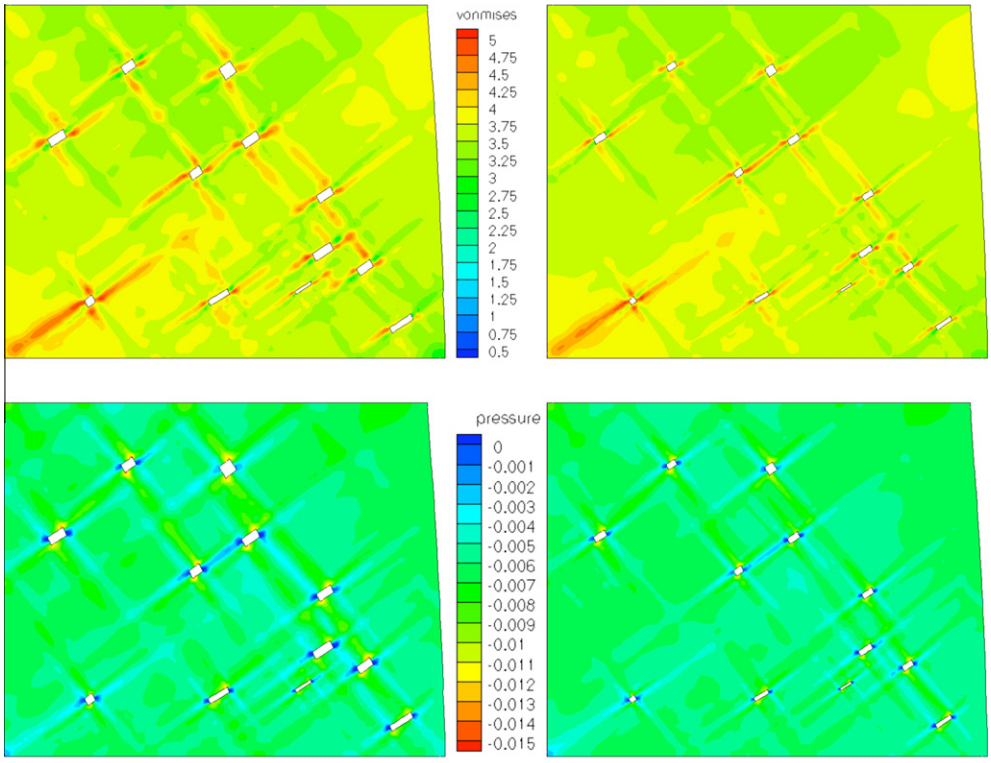

Fig. 4. von Mises stress (normalized by the matrix static yield stress) and pressure (normalized by the matrix Young's modulus) contours in the matrix at a 10% nominal compressive strain for particles aligned parallel to the most active slip plane: (a) 1.0% volume fraction, 800 nm by 425 nm average dispersed particle size and (b) 0.5% volume fraction, 600 nm by 300 nm average dispersed particle size.

$$g^{\alpha}_{immob-} = \frac{l_c f_0}{\sqrt{\rho^{\alpha}_{im}}} \sum_{\beta} \rho^{\beta}_{im}, \tag{6c}$$

$$g^{\alpha}_{mnter+} = \frac{l_c f_0}{\dot{\gamma}^{\alpha} \rho^{\alpha}_{m}} \sum_{\beta,\gamma} n^{\beta\gamma}_{\alpha} \left[\frac{\rho^{\gamma}_{m} \dot{\gamma}^{\beta}}{b^{\beta}} + \frac{\rho^{\beta}_{m} \dot{\gamma}^{\gamma}}{b^{\gamma}} \right], \tag{6d}$$

$$g^{\alpha}_{immob+} = \frac{l_c f_0}{\dot{\gamma}^{\alpha} \sqrt{\rho^{\alpha}_{im}}} \sum_{\beta} n^{\beta\gamma}_{\alpha} \rho^{\gamma}_{im} \dot{\gamma}^{\beta}, \tag{6e}$$

$$g^{\alpha}_{recov} = \frac{l_c f_0}{\dot{\gamma}^{\alpha}} \left(\sum_{\beta} \frac{\dot{\gamma}^{\beta}}{b^{\beta}} \right) e^{\left(\frac{-H_0 \left(1 - \sqrt{\frac{\rho^{\alpha}_{im}}{\rho_s}} \right)}{kT} \right)}. \tag{6f}$$

2.2. Orowan looping

The calculation of interfacial unrelaxed plastic strain is based on an eigenstrain formulation. The velocity gradient in the particle elements (elastic particles), coupled to the dislocation density based finite element formulation above, can be additively decomposed as

$$L_{kl} = L^{e}_{kl} + L^{*}_{kl}, \tag{7}$$

where L^{*}_{kl} is the eigenvelocity gradient.

The eigenvelocity gradient in each particle due to the plastic deformation of the surrounding matrix is taken as the negative of the volume average of the plastic velocity gradient of the surrounding matrix grain (see, for example, Mura, 1987).

$$L^{*}_{kl} = \frac{1}{V_{matrix}} \int_{V_{matrix}} L^{p}_{matrix} dV \tag{8}$$

The stress update is then cast using the eigenstrain rate tensor as

$$\sigma^{\Delta,lattice}_{ij} = C_{ijkl}(D_{kl} - D^{*}_{kl}) \tag{9}$$

2.3. Plastic relaxation

For particles larger than approximately 100 nm, as is the case with the $Al_{20}Cu_2Mn_3$ dispersed particles (Lee and Zikry, 2011a), relaxation of this eigenstrain in the particle will occur due to dislocation generation at the interface (Humphreys, 1979). The effect of this dislocation generation can be captured by relating the lattice rotations of the particles to that of the surrounding matrix grains.

Therefore, to represent the relaxation of the eigenstrain, the eigenvelocity gradient, L^{*}_{ij} is determined from the plastic velocity gradient of the surrounding matrix grain L^{p}_{ij} using Eq. (8), and it is relaxed based on the mismatch in the lattice rotations of the particles and the surrounding matrix grain when the eigenstrain $(\int D^{*}_{12,\max shear\_relaxed} dt)$ reaches a threshold of 0.1% to approximate the value at which a single Orowan loop would form for particles of this length scale (Brown and Stobbs, 1971, Eq. 1). The relaxation rate of the eigenstrain is determined by Eq. (10) as

$$\dot{\theta}_{relax} = sign(\bar{W}^{p}_{21matrix})(\dot{\theta}_{particle} - \dot{\theta}_{matrix}), \tag{10}$$

where the particle and matrix lattice rotations are averaged as

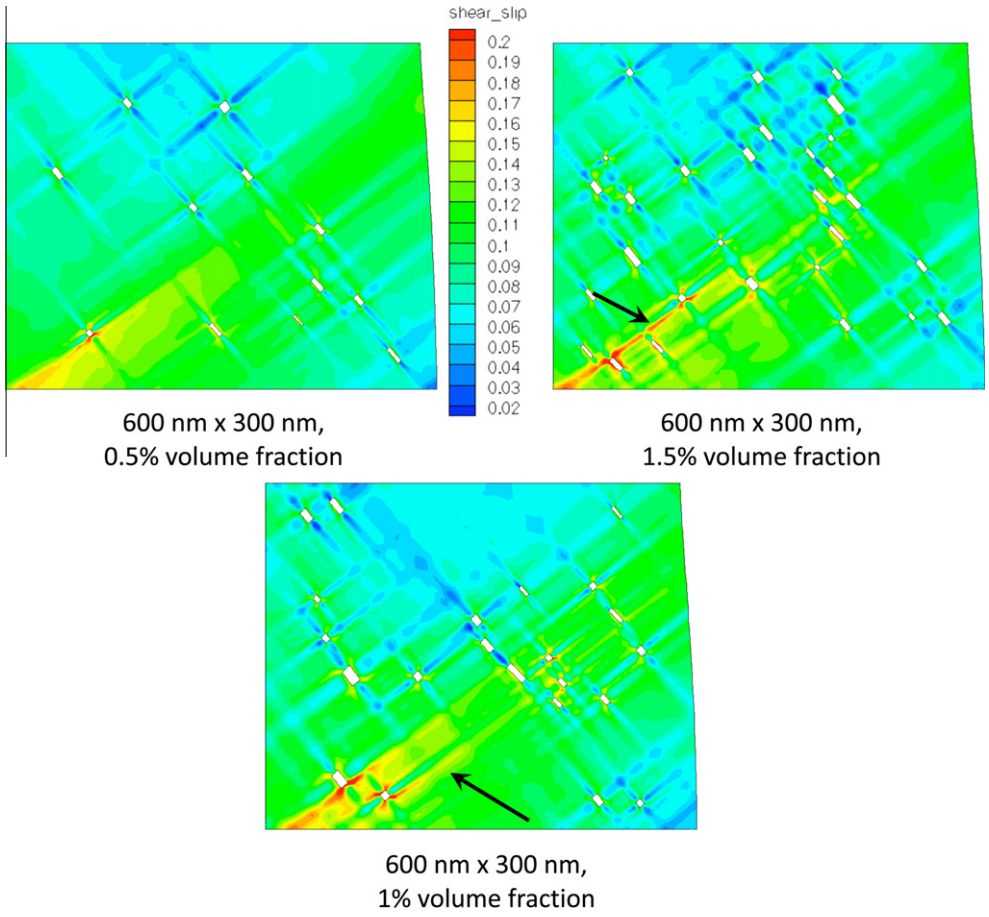

Fig. 5. Matrix effective plastic shear slip comparison at 10% nominal compressive strain for 600 nm by 300 nm average size particles normal to most active slip plane for 0.5%, 1.0% (arrow indicates banded slip), and 1.5% volume fraction (arrow indicates slip localization between particles).

$$\dot{\theta}_{particle} = \frac{1}{V_{particle}} \int_{V_{particle}} W^{e}_{21particle} dV,$$
$$\dot{\theta}_{matrix} = \frac{1}{V_{matrix}} \int_{V_{matrix}} W^{e}_{21matrix} dV,$$
$$\bar{W}^{p}_{21matrix} = \frac{1}{V_{matrix}} \int_{V_{matrix}} W^{p}_{21matrix} dV. \tag{11}$$

This relaxation is associated with the shear part of the eigenstrain. Therefore, implementation requires rotating the eigenstrain rate tensor to the maximum shear strain rate configuration to obtain $D^{*}_{\max shear}$. The maximum shear eigenstrain rate component is then

$$D^{*}_{12,\max shear} = \sqrt{\frac{1}{4}(D^{*}_{11} - D^{*}_{22})^{2} + D^{*2}_{12}}, \tag{12}$$

where this maximum shear is always taken as positive to correspond with the positive angular rate of relaxation (Eq. (10)). The relaxation rate is subtracted from the maximum shear eigenstrain rate tensor as

$$D^{*}_{\max\ shear\_relaxed} = D^{*}_{\max\ shear} - \begin{bmatrix} 0 & 1 \\ 1 & 0 \end{bmatrix} \frac{\dot{\theta}_{relax}}{2}. \tag{13}$$

The antisymmetric part of the eigenvelocity gradient is updated due to relaxation and is

$$W^{*}_{21relaxed} = W^{*}_{21} - sign(W^{*}_{21}) \frac{\dot{\theta}_{relax}}{2} \tag{14}$$

This relaxation is calculated only when the term $\dot{\theta}_{relax}$ is positive, accounting for the possibility of dislocation activity at the interface that does not relax the eigenstrain associated with Orowan looping.

2.4. Computational approach

The finite element techniques employed follow the formulation of Zikry (1994), and will be briefly outlined here. The velocity gradient of each element, L_{ij}, and the plastic (matrix) or eigen (particle) velocity gradient, L^{p}_{ij} or L^{*}_{ij}, are needed to update the stress state of the element through the Jaumann stress rate aligned with the crystal lattice by the use of the respective deformation rate and spin rate components. An implicit Newmark-β iterative approach using BFGS and one point Gauss quadrature is used to obtain the velocity gradient tensor, L_{ij}, for dynamic analyses. Values of $\beta = 1/4$ and $\gamma = 1/2$, corresponding to the trapezoidal rule, were chosen for unconditional stability. An implicit iterative approach using BFGS and one point Gauss quadrature were used for the quasi-static analyses. To overcome numerical stiffness issues, hybrid Runge–Kutta explicit and back Euler implicit method is used to solve for the resolved stresses, which are used to calculate the plastic components of the deformation rate and spin rate tensors. This hybrid scheme is also used to update the immobile and mobile dislocation densities. Stiffness based hourglass control is implemented to control numerical instabilities which can be triggered by the presence of dispersed particles and localized plastic slip (Lee and Zikry, 2011b).

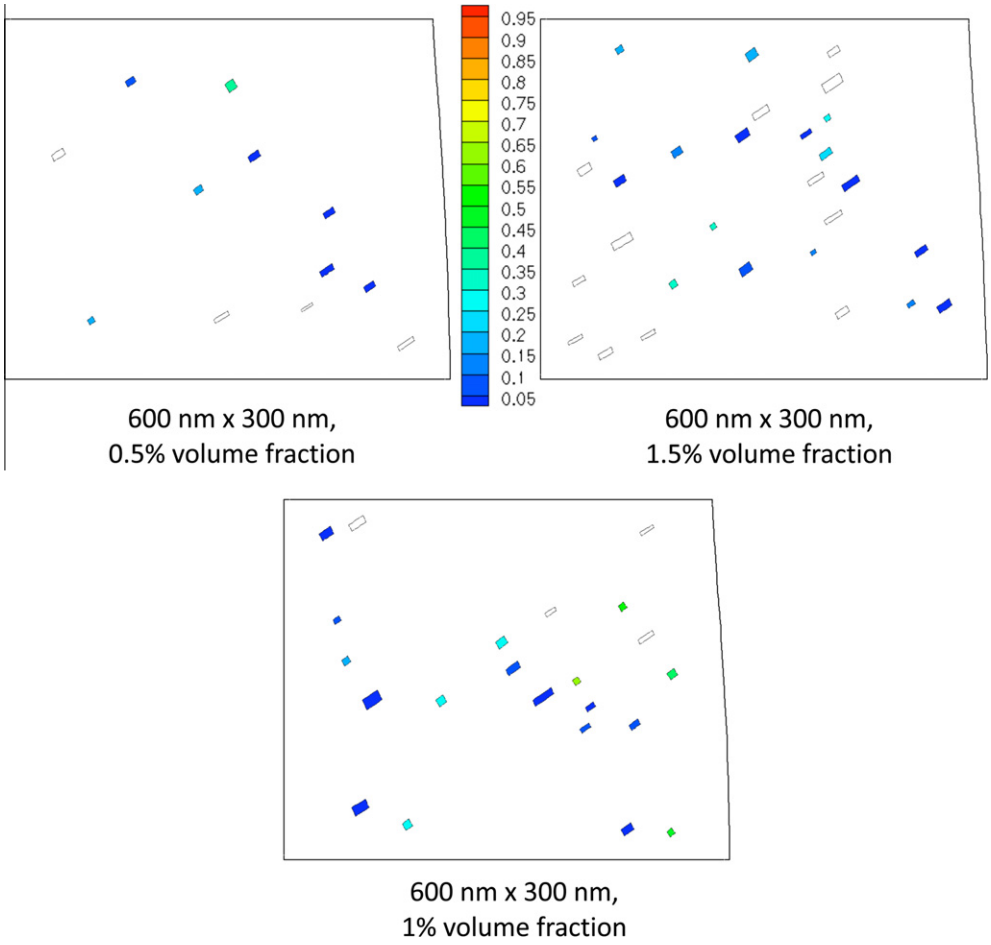

Fig. 6. Percent of eigenstrain relaxed $((\int D^{*}_{12,\max shear}dt - \int D^{*}_{12,\max shear\_relaxed}dt)/\int D^{*}_{12,\max shear}dt)$ at 10% nominal compressive strain for 600 nm by 300 nm average size particles parallel to the most active slip plane for 0.5%, 1.0% and 1.5% volume fractions.

3. Results

3.1. Microstructural representation

We investigated two high strain rate cases. The first investigated case was a 20 μm by 20 μm single crystal, modeled in adiabatic plane strain, subjected to a compressive strain-rate of $50 \times 10^3\ s^{-1}$ with different particle dispersions and particle sizes. The effects of particle spacing were investigated by modeling 1.0% volume fraction of randomly distributed dispersed particles with different particle sizes. The particle sizes were generated by a Gaussian distribution about averages of 600 nm × 300 nm for the smaller particle spacing and 850 × 425 nm for the larger particle spacing. The effects of particle size were investigated by modeling different particle sizes while maintaining the same particle distribution. Particles were randomly distributed and sized about an average of 600 nm × 300 nm to account for a volume fraction of 0.5%, and scaled up to 850 nm × 425 nm to account for a volume fraction of 1.0% to investigate larger particle sizes. Finally, volume fraction effects were investigated using randomly distributed particles sized about the experimentally observed mean of 600 nm by 300 nm (Lee and Zikry, 2011a) at volume fractions of 0.5%, 1.0%, and 1.5%. The matrix lattice was aligned for preferential slip along the (1–11) plane as indicated in Fig. 1 with Euler angles of $\varphi_1 = 45^{\circ}$, $\Phi = -19.7^{\circ}$, and $\varphi_2 = 0.0^{\circ}$. Symmetry boundary conditions were used and two dispersed particle configurations were investigated: (i) the long axis of all particles aligned parallel to the initially preferential slip plane of (1–11), and (ii) the long axis of all particles aligned normal to the initially preferential (1–11) slip plane. Symmetry BC's crystallographically can represent high misorientation grain boundaries, leading to high stress concentrations and localization initiated at the bottom left corner. The localization will proceed at the angle of maximum macroscopic shear stress, which makes the localization propagate to the upper right corner. A mesh of approximately 18,600 elements was used with a minimum of three elements along each particle side.

The second case that was investigated was 20 μm by 20 μm polycrystalline aggregates with randomly oriented and sized particles to understand how and whether grain orientations affect interfacial behavior pertaining to the dispersed particles. Three aggregates with a distribution of one particle per grain to account for a 1.0% volume fraction were investigated: a 20-grain aggregate with an average particle size of 600 nm × 300 nm, a 35-grain aggregate with an average particle size of 500 nm × 250 nm, and a 48-grain aggregate with an average particle size of 400 nm × 200 nm. Random high angle and low angle GB misorientations between the crystal grains were used. Table 1 summarizes the average grain misorientations for each scenario. A strain-rate of $50 \times 10^3\ s^{-1}$ with plane strain adiabatic compression and symmetry boundary conditions was used. An isothermal quasistatic case with a strain-rate of $0.004\ s^{-1}$ was also conducted to fully understand how variations in strain-rate affect behavior. A mesh of approximately 16,000 elements was used, with a minimum of three elements along each particle side. Fig. 1 summarizes the models used for the two cases. The properties of the particles and matrix grains are summarized in Table 2.

3.2. Single grain

3.2.1. Particle spacing effects

The effects of particle spacing were investigated for a 1.0% volume fraction of randomly distributed dispersed particles with different average particle sizes of 600 nm × 300 nm (smaller spacing) and 850 nm × 425 nm (larger spacing) as shown in Fig. 1a. The contours of effective plastic shear slip for particles aligned parallel to and normal to the most active slip plane are shown in Fig. 2. For both particle alignments, with more closely spaced dispersed particles, the effective shear slip develops into three slip bands that extend to approximately one-third of the crystal, as compared to the more diffuse shear slip associated with the larger particle spacing. This indicates that the spacing of particles has a pronounced effect on the shear slip distribution.

Fig. 3 details the pressure distribution for the different particle spacings. It is evident that for the models with particles aligned parallel to the most active slip plane (Fig. 1), tensile pressures accumulate at the particle matrix interface to a greater extent than for the particles aligned normal to the most active slip plane. Particle interactions can also be clearly seen for the particles aligned parallel to the most active slip plane. The compressive pressures between the particles are smaller than the mean value in the matrix. This reduction in the compressive pressures can promote faster void coalescence once voids are nucleated at the particle/matrix interface. This effect is more pronounced for the larger particles (Fig. 3).

3.2.2. Particle size effects

The effects of particle size were investigated for particles with an average size of 600 nm by 300 nm with a volume fraction of 0.5%, and for particles with an average size of 850 nm by 300 nm with a 1.0% volume fraction in a single 20 μm by 20 μm crystal (Fig. 1a). The pattern of shear slip is largely unaffected by particle size, but the intensity of plastic shear slip increases as the particle size increases, with plastic strains that are generally larger than those associated the smaller dispersed particles. This is due to the difference in stress accumulations for the particles of different sizes, as can be seen from the von Mises stress and pressure contours of Fig. 4. The larger dispersed particles generally have larger accumulations near the interfaces of the dispersed particles.

This difference in stress accumulations can be understood in terms of the unrelaxed plastic strain at the interfaces of the dispersed particles. The eigenstrain in each particle initially is the negative of the plastic strain in the surrounding matrix grain (Eq. (8)). For both particle sizes, the amount of plastic relaxation was similar. Therefore, the relaxed eigenstrain in each particle is similar. The eigenstrain is proportional to the number of Orowan loops and the particle size (Brown and Stobbs, 1971), with the number of Orowan loops increasing with particle size. The loops lead to a greater eigenstresses, and therefore greater stress accumulations at the particle matrix interface.

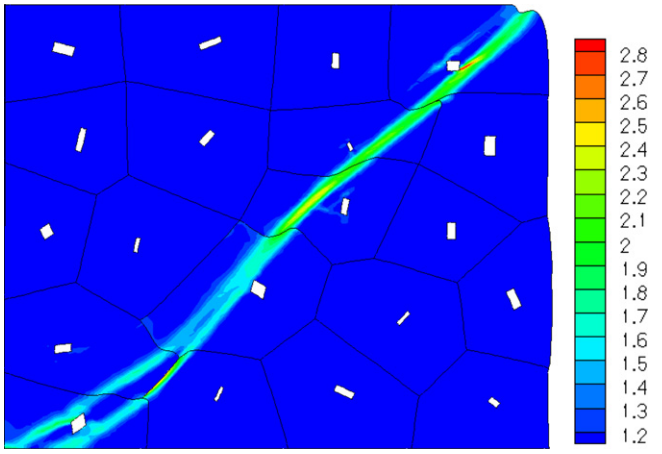

Fig. 8. Matrix temperature (normalized by 293 K) at 10% nominal compressive strain for the 20-grain aggregate with the eigenstrain formulation at a strain rate of 50,000 s^{-1}.

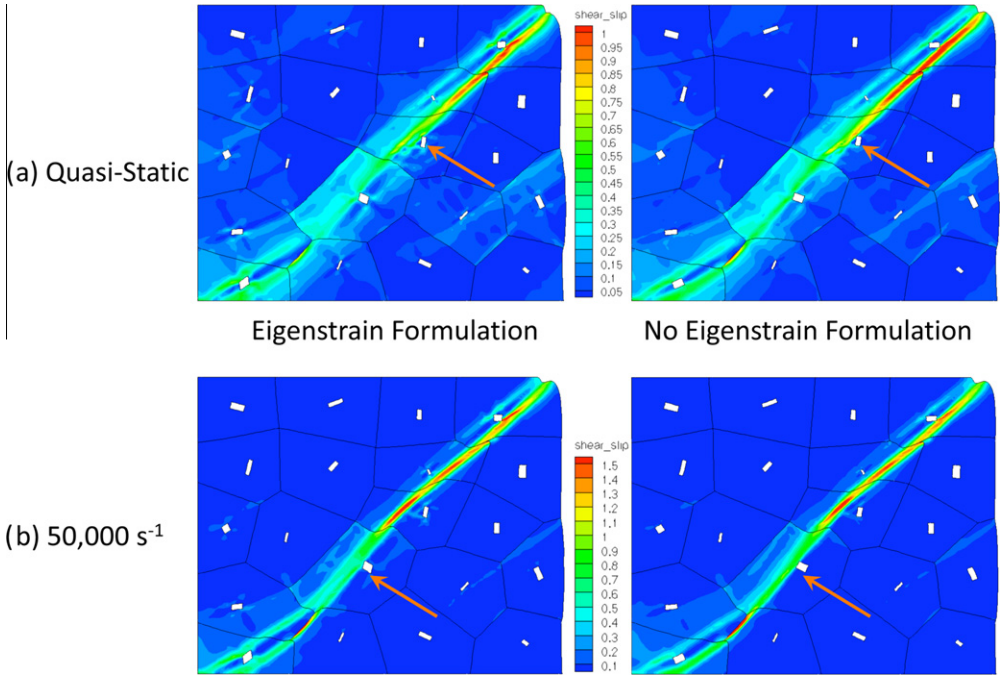

Fig. 7. Comparison of effective plastic shear slip in the matrix at 10% nominal compressive strain for a 20-grain aggregate with high angle GB misorientations with and without the eigenstrain formulation included at (a) quasi-static (0.004 s^{-1}) and (b) 50,000 s^{-1} strain rates.

The effect of these greater eigenstresses can be seen by the pressure contours of Fig. 4. The interaction between the particles, leading to decreases in the compressive pressures between the larger particles, can enhance the nucleation and eventual coalescence of voids, which indicates that smaller particles may be beneficial in delaying final void coalescence. This underscores that particle size and spacing have a critical role in failure evolution.

3.2.3. Volume fraction effects

The effects of volume fraction were investigated by comparing particle dispersions with volume fractions of 0.5%, 1.0%, and 1.5% and an average particle size of 600 nm by 300 nm in a single 20 μm by 20 μm single crystal (Fig. 1a). The volume fraction clearly affects the pattern of plastic slip, which can be seen in Fig. 5, for particles initially aligned normal to the most active slip plane. For the 0.5% volume fraction, the particle effects on the shear slip distribution are minimal, since there is a larger particle spacing (Fig. 5, see also Fig. 2b). As the volume fraction is increased to 1%, the shear slip forms a banded distribution, with distinct bands associated with the dispersed particles (Fig. 5). As the particle spacing is reduced due to the further increase of volume fraction to 1.5%, the shear slip becomes highly localized between the particles, which can lead to the onset of shear failure between the particles, with shear band initiation at the particle/matrix interface.

The effect of volume fraction on the relaxation of the eigenstrain can be seen in Fig. 6. For particles aligned parallel to the most active slip plane, which show little relaxation for all cases, there is a much greater percentage of particles that do not relax for the highest volume fraction of 1.5%. This indicates that as the volume fraction increases, relaxation becomes more difficult. This effect was greater for the particles aligned parallel to the most active slip plane than those aligned normal to the most active slip plane.

3.3. Polycrystalline aggregate and dispersed particle distributions

To investigate the interrelated effects of dispersed particles and grain orientations, three 20 μm by 20 μm polycrystalline aggregates were studied: a 20-grain aggregate with an average particle size of 600 nm × 300 nm, a 35-grain aggregate with an average particle size of 500 nm × 250 nm, and a 48-grain aggregate with an average particle size of 400 nm × 200 nm. In each case, the particle volume fraction was 1%, and both random high angle and random low angle GB misorientations were investigated (Table 2). Fig. 7 compares the behavior of the high angle 20-grain aggregate for compressive strain-rates of $4 \times 10^{-3}\,s^{-1}$ and $50{,}000\,s^{-1}$ with and without the eigenstrain formulation to determine how strain rate variation affects eigenstrains.

For all the cases, a shear band develops at the triple junction located at the bottom left of the top right grain. The band propagates to the free boundary bypassing the dispersed particle near the free boundary at the particle-matrix interface. The propagation of the band in the other direction depends on the strain rate and whether or not the eigenstrain formulation is included in the simulation. Under quasi-static loading conditions, without the eigenstrain, the band propagates to the interface of the particle marked by an arrow in Fig. 7a. When the eigenstrain formulation is included, the eigenstress field associated with the eigenstrain alters the path

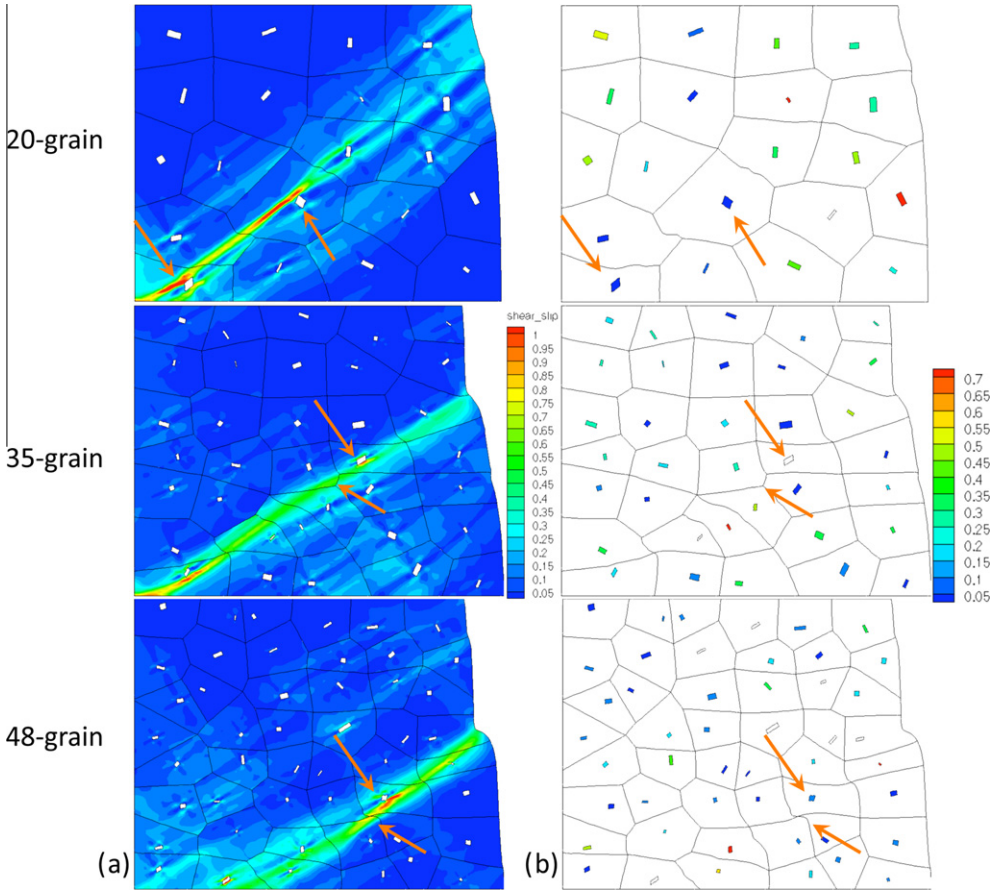

Fig. 9. (a) Effective plastic shear slip in the matrix and (b) percent of eigenstrain relaxed at 10% nominal compressive strain for the 20-, 35-, and 48-grain aggregates with low angle GB misorientations.

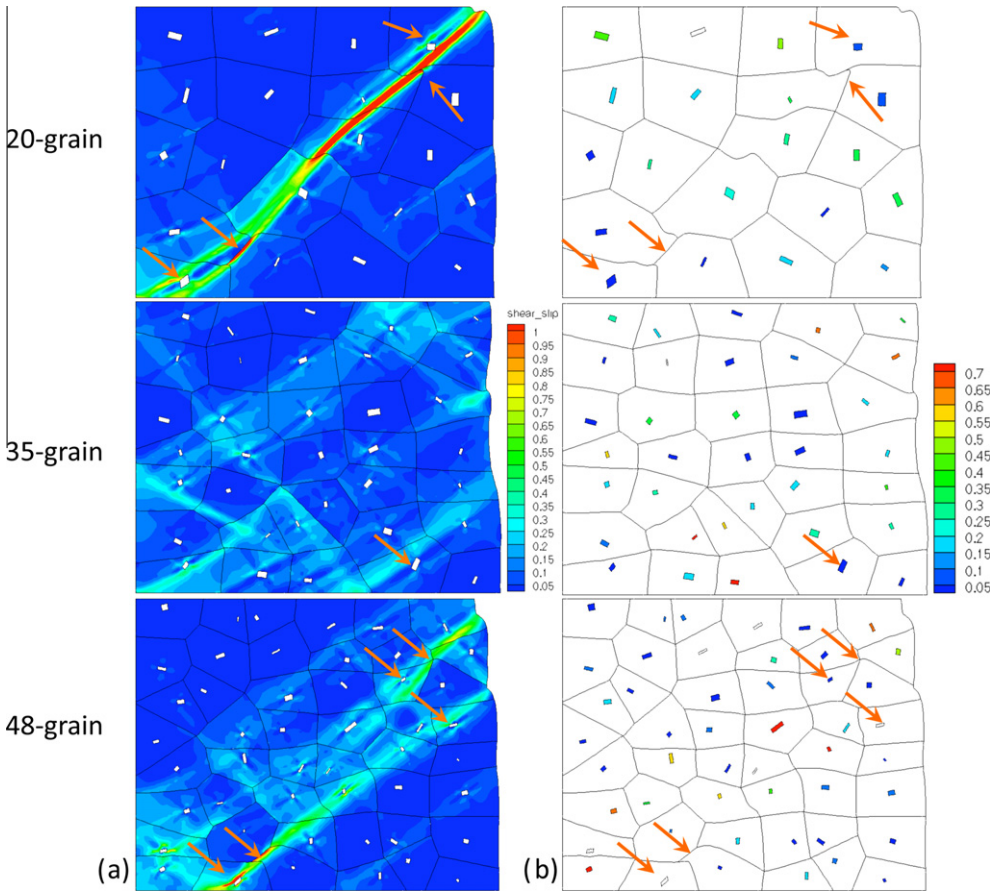

Fig. 10. (a) Effective plastic shear slip in the matrix and (b) percent of eigenstrain relaxed at 10% nominal compressive strain for the 20-, 35-, and 48-grain aggregates with high angle GB misorientations.

of the shear band away from the particle, which also reduces the intensity of the band.

The difference in the two bands, for the strain-rate of 50,000 s^{-1}, with and without the eigenstrain, is minimal in comparison with the quasi-static cases. Some broadening of the band is seen near the particle marked by an arrow in Fig. 7b. However, the general path of the band is largely unaffected by the eigenstrains. This indicates that the effects of thermal softening, which occurs due to the temperature rise associated with the high strain rate deformation (Fig. 8), may be more dominant than the eigenstrain effects. As evident from Fig. 8, there is considerable thermal accumulation within the band.

The effects of the grain orientations and eigenstrain relaxation can be seen in for low angle (Figs. 9) and for high angle (Fig. 10) GB misorientations. For all low angle GB aggregates, slip localizes to some extent in the general orientation of the most active slip plane (see Fig. 2b). For the 20-grain aggregate, plastic shear slip localization occurs at the particle matrix interface of two particles that are associated with the lowest relaxation (Fig. 9b). The localization does not fully extend to the free boundary, where the particles near the free boundary do relax. The local deformation behavior of the 35-grain and 48-grain low angle aggregates is associated with particles that minimally relax and at grain junctions of 3 and 4 grains. It is also evident that the highest effective plastic shear slip values occur at the particle/matrix interfaces.

Similar trends can be seen for the high angle GB aggregates (Fig. 10). Highly localized deformation occurs for the 20-grain and 48-grain aggregates at the GBs, at grain junctions, and at particle/matrix interfaces of particles where the eigenstrain does not relax. Minimal localization is seen for the 35-grain aggregate, but some local behavior (See arrows, Fig. 10a) is associated with a particle that shows minimal relaxation. The major difference between the deformation of the low angle and high angle GB aggregates is the interrelated effects of the particles and the GBs. The deformation of the low angle GB aggregates is associated with more local shear slip (Fig. 9a) behavior at the particle/matrix interface, whereas the deformation of the high angle grain aggregates is more local at the GBs and grain junctions. The GBs at the lower left of the 20-grain and 48-grain aggregates are associated with highly localized shear slip, as is the triple junction at the top right of the 20-grain aggregate. These bands propagate to the interfaces of particles for which the matrix does not relax the eigenstrain.

4. Conclusions

An eigenstrain formulation accounting for incompatibilities in plastic strain associated with Orowan looping and plastic relaxation coupled to a dislocation-density based crystalline plasticity and a microstructurally-based finite-element framework was used to investigate the interrelated effects of particle dispersion, orientation, size and spacing, and GB misorientations for a high strength aluminum alloy subjected to high strain rate deformation. Particle spacing had a significant effect on plastic shear slip distribution, with interaction between the particles, including shear slip localization and decreasing compressive pressure fields, occurring for smaller spacing. Larger particles had a greater effect on the stress fields near the particle/matrix interfaces, which led to longer range interaction of particle stress fields, including the tendency for more

decreasing compressive pressure fields developing between particles, which can enhance void nucleation and eventual coalescence.

For the polycrystalline aggregates with dispersed particles, shear strain localization occurred as a function of the particle eigenstrain, GB misorientations, and thermal softening. For low angle GB misorientations, shear strain localization can be triggered at the particle/matrix interfaces of particles where the eigenstrain is not relaxed. High angle GB misorientations led to the onset of shear slip localization, occurring first at GBs and grain junctions, and propagating to the particle-matrix interface of particles where the eigenstrains were not relaxed.

Acknowledgements

Support from JIEDDO and the U.S. Army Research Office Grant No. ARO W911 NF-06–1–0472 are gratefully acknowledged. W.M. Lee also acknowledges support from the National Defense Science and Engineering Graduate (NDSEG) Fellowship.

References

Ashmawi, W.M., Zikry, M.A., 2000. Effects of grain boundaries and dislocation density evolution on large strain deformation modes in FCC crystalline materials. J. Comp.-Aided Mater. Des. 7, 55–62.

Bacon, D.J., Osetsky, Y.N., 2005. Modeling dislocation-obstacle interactions in metals exposed to an irradiation environment. Mater. Sci. Eng. A. 400, 353–361.

Bacon, D.J., Osetsky, Y.N., 2007. The atomic-scale modeling of dislocation-obstacle interactions in irradiated metals. J. Mater. 59, 40–44.

Bate, P., 1999. Modeling deformation microstructure with the crystal plasticity finite-element method. Phil. Trans. Royal Soc. Lon. A. 357, 1589–1601.

Brown, L.M., Stobbs, W.M., 1971. The work-hardening of copper-silica I. A model based on internal stresses, with no plastic relaxation. Phil. Mag. 23, 1185–1199.

Cho, A., Bes, B., 2006. Damage tolerance capability of an Al–Cu–Mg–Ag alloy (2139). Mater. Sci. Forum 519–521, 603–608.

Elkhodary, K.I., Lee, W.M., Sun, L., Brenner, D.W., Zikry, M.A., 2011. Deformation mechanisms of an Ω precipitate in a high strength aluminum alloy subjected to high strain rates. J. Mater. Res. 26, 487–497.

Hatano, T., 2008. Dynamics of a dislocation bypassing an impenetrable precipitate: the hirsch mechanism revisited. Phys. Rev. B. 74, 1–4.

Humphreys, F.J., Stewart, A.T., 1972. Dislocation generation at SiO_2 particles in an – brass matrix on plastic deformation. Surface Sci. 31, 389–421.

Humphreys, F.J., 1979. Local lattice rotations at second phase particles in deformed metals. Acta Metall. 27, 1801–1814.

Kameda, T., Zikry, M.A., 1998. Three dimensional dislocation-based crystalline constitutive formulation for ordered intermetallics. Scripta Metall. Mater. 38, 631–636.

Kohler, C., Kizler, P., Schmauder, S., 2005. Atomistic simulation of precipitation hardening in alpha-iron: influence of precipitate shape and chemical composition. Model. Sim. Mater. Sci. Eng. 13, 35–45.

Lee, W.M., Zikry, M.A., 2011a. Microstructural characterization of a high-strength aluminum alloy subjected to high strain-rate impact. Metall. Mater. Trans. A. 42, 1215–1221.

Lee, W. M., Zikry, M. A. Microstructurally induced hourglass modes. Comp. Mech. Submitted for publication

Mura, T., 1987. Micromechanics of Defects in Solids, second ed. Martinus Nijhoff, Netherlands.

Queyreau, S., Devincre, B., 2009. Bauschinger effect in precipitation-strengthened materials: a dislocation dynamics investigation. Phil. Mag. Letters 89, 419–430.

Salem, H.A.G., Lee, W.M., Bodelot, L., Ravichandran, G., Zikry, M.A., 2012. Quasi-static and high strain-rate experimental microstructural investigation of a high strength aluminum alloy. Metall. Trans. A. 43A, 1896–1901.

Shanthraj, P., Zikry, M.A., 2011. Dislocation density evolution and interactions in crystalline materials. Acta Mater. 59, 7695–7702.

Shim, J.-H., Kim, D.-I., Jung, W.-S., Cho, Y.W., Hong, K.T., Wirth, B.D., 2008. Atomistic study of temperature dependence of interaction between screw dislocation and nanosized BCC Cu precipitate in BCC Fe. J. Appl. Phys. 104, 083523.

Starke, E. A., Sanders, T. H., 1980. The effect of microstructure on the properties of high strength aluminum alloys. AFOSR Annual Scientific, Report. ADA083768.

Takahashi, A., 2008. Parameteric dislocation dynamics and boundary element modeling of elastic interaction between dislocations and precipitates. NATO Science for Peace and Security Series B – Physics and, Biophysics. pp. 263–274.

Zikry, M.A., 1994. An accurate and stable algorithm for high strain-rate finite strain plasticity. Comp. Struct. 50, 337–350.

Zikry, M.A., Kao, M., 1996. Inelastic microstructural failure mechanisms in crystalline materials with high angle grain boundaries. J. Mech. Phys. Solids 44, 1765–1798.